Dynamical level-crossing model for the time-dependent electron emission from dielectric surfaces in symmetric dielectric barrier discharges

Purnima Ghale and Harley T. Johnson*
Department of Mechanical Science and Engineering, University of Illinois at Urbana-Champaign, Urbana, Illinois 61801, USA

(Received 3 December 2018; revised manuscript received 27 February 2019; published 4 April 2019)

In field emission plasmas, electrons that initiate plasma formation come from the surface of a metallic electrode, or wall, with emission controlled by the electron-work function of the wall, and can be computed via the Fowler-Nordheim formula. Impinging ions modify the rate at which electrons leave the surface, and are accounted via the coefficient of secondary electron emission. However, in the case of dielectric surfaces, the microscopic mechanism by which electrons are emitted is not as well understood. While simulations of dielectric barrier discharge plasmas assume an initial density of electrons in a time-dependent simulation, whether the presence of electrons is a necessary ambient condition or whether it is a result of emission from a surface is not clear. This is particularly relevant in the context of micro and nanoscale plasma generators when surface-related effects become more important. Here we consider electron emission from dielectric surfaces in the context of dielectric barrier discharges. The configuration of interest consists of two parallel-plate metallic electrodes, each covered by a dielectric layer. Assuming that the initial electrons for plasma formation arise from the surface, we compute the rate of charge transfer from surfaces, which is a necessary, but not sufficient, condition for plasma formation. This paper presents the application of the theory of nonadiabatic transitions (dynamical level crossing) to the problem of electron emission from dielectric surfaces in dielectric barrier discharges. The microscopic model of electron transfer described here has potential applications in the design of micro and nanoscale plasma generators.

DOI: 10.1103/PhysRevB.99.155405

I. INTRODUCTION

Dielectric barrier discharges (DBDs) have been used since the 19th century [1] and have applications in materials processing, ozone synthesis, plasma displays, combustion, and aerodynamic flow control [2–6]. A typical setup consists of an external ac voltage and at least one dielectric barrier between metallic electrodes. The configuration of interest in this paper is the symmetric planar DBD where both metallic electrodes are covered by a layer of dielectric dielectric material, like quartz, such that the gaseous region lies between the dielectric surfaces [7]. Electron emission of primary and secondary electrons from surface walls and electron-impact ionization in the gaseous region are requisite mechanisms for plasma generation [8–10]. In the simplest lumped element model or circuit model [11–14] used to investigate current-voltage behavior in DBDs at the device level, the dielectric-gas-dielectric system is modeled as a series of capacitors in the absence of plasma, and the formation of plasma in the gaseous region is denoted by a switch which adds a resistor to the previously capacitive circuit.

Alternatively, more detailed numerical models consisting of direct simulation Monte Carlo and particle-in-cell methods [15,16] have been developed to predict plasma generation in various operational regimes. These models solve the Boltzmann transport equation, and thus take the volumetric effect of electron-impact ionizations and diffusive loss mechanisms into consideration, but require an initial electron density and coefficient of electron emission from surfaces for closure [17]. The role of surfaces becomes more important as devices are miniaturized; already, micro- and nanoscale plasma generators have found a wide variety of applications [18], and microcombustion applications of asymmetric DBD plasmas, with one metallic and one dielectric surface, have been recently investigated [19]. In the case of direct-current field-emission plasmas, the connection between metallic electrodes and gaseous regions is well established—electron emission from surfaces has been investigated in the context of field and thermionic emission, and understood in terms of the Fowler-Nordheim formula [20,21], while the coefficient of secondary electron emission, γ_{se}, quantifies the effect of impinging ions on electron emission. In ac symmetric DBDs, however, metallic electrodes are each covered by a layer of insulating dielectric material, and the Fowler-Nordheim picture is complicated by the higher work function, large band gap, and localization of electronic states of dielectric materials like $\alpha-$quartz.

In this paper, semiempirical tight binding is used to obtain the electronic structure of the dielectric layers. Energies of gaseous atoms are obtained using density functional theory but they are used as quasiparticle states that can be occupied or unoccupied, as in tight binding. Given an electronic structure method of choice, one way to investigate the effects of a time-dependent external potential on electron emission would be to study the evolution of the many-particle wave function or density matrix [22,23]; while ideal, these methods are expensive for simulations of systems with thousands of

*htj@illinois.edu

states for hundreds of microseconds. Alternatively, the theory of nonadiabatic transitions (or Landau-Zener-Stückelberg [24–26] model) can be used to construct initial models of electron transfer during chemical reactions [27], and more recently has been used to investigate time-dependent electron transfer between quantum dots [28,29], as well as ionization of Rydberg atoms [30,31]. This paper presents the application of the theory of nonadiabatic transitions to investigate electron transfer between dielectrics and gases under ac voltage in the context of plasma generation. Our intuition behind this model of electron emission from dielectric surfaces is that in the absence of an external photon or phonon, degeneracies between occupied and empty states are required for electron transfer via tunneling. In the case of field-emission from metallic surfaces, the presence of an external dc field creates the degeneracy required for tunneling between conducting states inside the metal and free electron states outside, by bending the potential barrier faced by an electron at the metallic surface. In the case of dielectric-gas-dielectric systems under ac voltage, degeneracies between localized states within and outside the dielectric surface appear due to time-dependent energy level crossing, leading to the possibility of time-dependent electron transfer. The temporal profile of current-voltage phase lag, as well as surface charge accumulation and depletion obtained from our computations using simple energy-level crossing arguments, are consistent with experimental observations in the literature [32–35], but quantitative agreement with experiments requires more detailed computations coupling electron transfer from dielectric surfaces with the kinetics of plasma formation, and are beyond the scope of this paper.

Figure 1 presents a schematic diagram of the DBD device, in terms of the material components of the device. The metallic electrodes, which are reservoirs of charge carriers, and the gaseous region where charge carriers are necessary to initiate plasma formation, are separated by a dielectric layer of $\alpha-$quartz. When an external potential difference is applied, a linear potential drop is expected across various insulating parts of the device, according to their relative permittivity ϵ_r, and we are interested in the time-dependent transfer of electrons from the dielectric into the gaseous argon under a time-dependent potential $V_{\text{ext}}(t)$. The part of the system isolated by a dashed box is of interest in this paper—it consists of the argon region as well as thin layers of the dielectric material in contact with the gaseous region; we will use electronic structure calculations to obtain the quasiparticle states of this system.

Figure 2 shows the isolated system of interest both during plasma generation from the perspective of plasma physics [Fig. 2(a)], and also before plasma generation from the perspective of electronic structure theory[Fig. 2(b)]. First, Fig. 2(a) shows a schematic of surface-supported plasma during operation, where the horizontal axis represents the gap distance between the walls. In case of DBD plasmas, the metallic electrodes are covered by layers of dielectric material, which serve as the walls facing the gaseous region. The vertical axis represents the electrostatic potential, $V(r)$, experienced by the electrons and ions. Before plasma formation, the electrostatic potential $V(r)$ is linear; after plasma formation, the conducting plasma channel does not support a

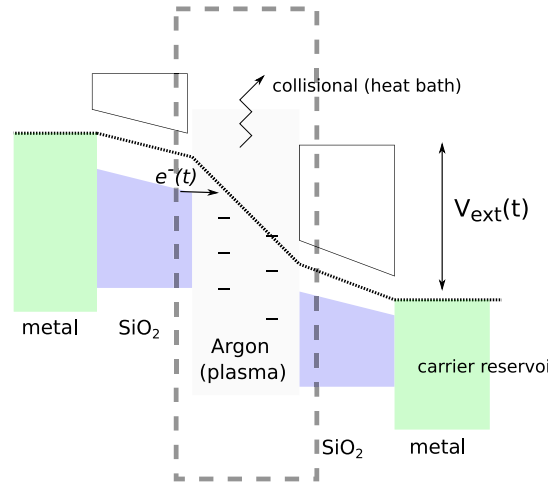

FIG. 1. The dielectric barrier discharge device in terms of its material components and the expected potential drops across the system (metal-dielectric-gas-dielectric-metal) as a time-dependent external potential difference $V_{\text{ext}}(t)$ is applied. The reservoirs of charge carriers (metallic electrodes) and the gaseous argon are separated by dielectric material (SiO_2). The region isolated by a dashed box is the system investigated in this paper and contains the surface regions of dielectric walls with gaseous argon in between. In the gaseous region, argon atoms are assumed to be stationary; the dissipative effects of the motion of argon atoms, denoted here in terms of a collisional heat bath, are not considered but are briefly discussed in Sec. II D.

voltage drop, and the potential difference applied between the walls results in the formation of a sheath region with a large potential drop near the walls. Figure 2(b) shows a schematic representation of energy levels in the dielectric-gas-dielectric system that exist before plasma formation. The horizontal axis represents the same distance as in Fig. 2(a) but the vertical axis represents the energy levels of the dielectric and gaseous materials in the absence of an external field. The valence and conduction bands of the dielectric form a continuum of states and are represented by filled blocks, while the effective single particle states of the gaseous atoms are shown by discrete lines. Gray or lightly filled smaller blocks in the dielectric region represent surface states that appear due to surface termination.

Finally, we note that the total number of electrons in the isolated system is held constant—as such, electron transfers result in charge depletion (holes) and accumulation (electrons) on the dielectric surfaces. The computation of charge depletion and accumulation complements recent phenomenological and experimental investigations of surface effects such as surface charge accumulation and depletion, memory effects on microdischarge formation, and surface charge transport [32,34,35]. However, surface charges can also be transported toward metallic contacts, and recent works have investigated electron absorption and subsequent transport in dielectric materials, and the associated effects of phonons and impurities [36–39]. This transport of charge carriers away from the isolated dielectric-gas-dielectric system can be coupled to charge transport within the isolated system, but is not the focus of this paper.

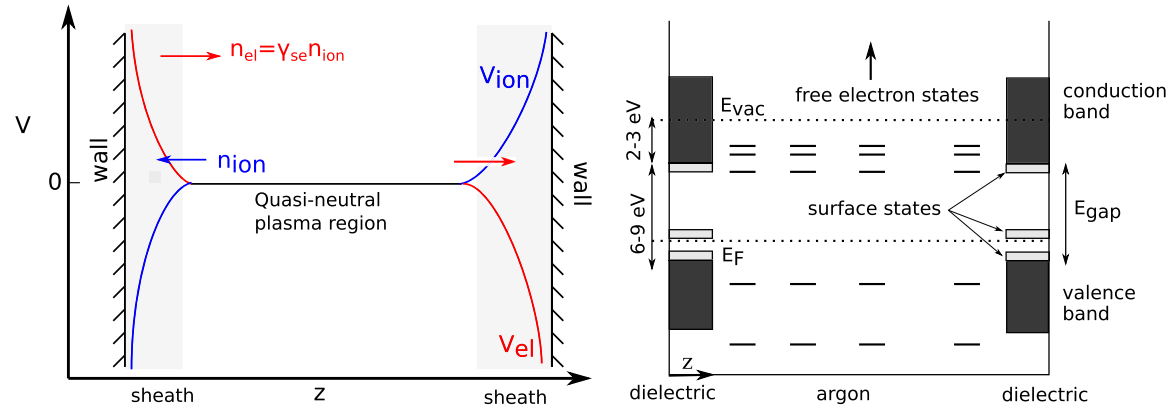

(a) Schematic during plasma operation

(b) Energy levels when $V_{ext} = 0$

FIG. 2. (a) Schematic of surface-supported plasma with the plasma sheath and quasineutral conducting channel shown. The horizontal axis represents the z distance along which the external field is applied; the vertical axis denotes the electrostatic potential experienced by electrons and positive ions, respectively. (b) Simple model of electronic states, where the y axis denotes the individual energy levels of the effective quantum mechanical system. The wall is mapped onto the energy levels associated with the dielectric, which is represented by dense bands; energy levels associated with gaseous atoms in the intermediate region are shown as discrete lines.

The outline of this paper is as follows: Sec. II presents an atomistic description of the methods used and materials considered. The electronic structure parametrizations, multistate energy level crossings within the theory of nonadiabatic transitions, and approximations that allow us to compute the rate of charge transfer in our system of interest are discussed. Next, results of our calculations are presented in Sec. III, where we first present the density of states of the dielectric layers, followed by the predicted charge transfers in the limit that the system varies infinitely slowly, within the adiabatic approximation. In the same section, multistate energy level crossings are presented, and the rates of electron transfer are computed by using the theory of nonadiabatic transitions. Finally, conclusions are presented in Sec. IV.

II. METHODS AND MATERIALS

A. Description of the system

The atomistic system of interest consists of two dielectric layers separated by a gaseous region as shown in Fig. 3, where atomic layers of $\alpha-$quartz represent only a small fraction of the dielectric material near the surface, facing gaseous argon along the gap distance between dielectric walls. The extent of the dielectric material is limited to a $3 \times 3 \times 3$ lattice of right-handed $\alpha-$quartz with Si and O termination in the 0001 direction, and with periodic boundary conditions in the x and y directions. Next to the gaseous region, the surfaces facing the argon gas and the resulting plasma are represented by the O-terminated quartz stabilized by hydrogenation. Away from the gaseous region, the dielectric layers extend to metallic electrodes as shown in Fig. 1, which drives the system by applying the total voltage $V_{\text{total}}(t)$. Between metallic contacts, the voltage drops linearly along the z direction based on the relative permittivity, ϵ_r, of the medium. A part of this potential difference occurs between the dielectric layers, and is taken as the external potential difference for the system shown in Fig. 3, $V(t) = V_0 \sin \omega t$ along the z direction. Finally, $\Delta =$ 17 Å in Fig. 3 denotes the thickness of the dielectric layer considered, and the gap between walls, d_{gap}, is set to at least 100Δ.

B. Electronic structure

A collisionless nonreactive model for gaseous argon is used, with single-particle electron energy levels, ϵ_i^0, set equal to the Kohn-Sham energies from density functional theory, obtained using the ATOM code distributed with SIESTA [40,41], using the local density approximation [42]. Energies corresponding to the closed-shell configuration with an sp^3 $(4s, 3d, 5p)$ basis are used for the Ar atoms. The electronic structure of $\alpha-$quartz is computed using semiempirical tight binding parameterized [43,44] for silicon, oxygen, and hydrogen atoms. The sp^3 orbital set is used for Si and O atoms, and a $1s$ orbital is used to characterize H. Interorbital interactions between argon orbitals and quartz are set to zero. The following total Hamiltonian, in the absence of other

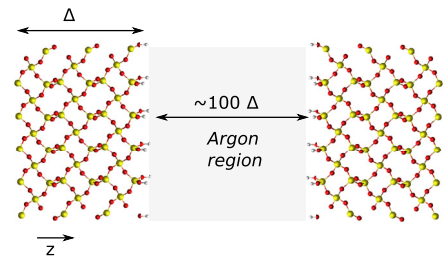

FIG. 3. Atomistic description of the system of interest showing dielectric layers ($\alpha-$quartz) and the gaseous region (Ar atoms) in between. The 0001 surface with $-$OH termination is exposed to the gaseous region. Away from the gaseous region, the dielectric layer extends beyond the few atomic layers shown here to metallic contacts. Periodic boundary conditions are used in the x and y directions. Here, Δ denotes the thickness of the dielectric layer considered. The gap distance between walls is on the order of 100Δ or more.

external potentials and interstate coupling, is used:

$$H^0 = \begin{bmatrix} H^{\rm tb} & 0 & 0 \\ 0 & H^{\rm Ar} & 0 \\ 0 & 0 & H^{\rm tb} \end{bmatrix}, \tag{1}$$

where $H^{\rm tb}$ denotes the tight-binding Hamiltonian for $\alpha-$quartz, and $H^{\rm Ar}$ denotes the diagonal Hamiltonian containing single-particle energies of Ar. Single-particle states, ψ_i, are expressed as linear combinations of atomic orbitals, or

$$\psi_i(\vec{x}) = \sum_{m=1}^{N} c_{im}\phi_m(\vec{x} - R_A), \tag{2}$$

where ϕ_m are atomic orbital bases centered around atoms A, while c_{im} are the coefficients of linear expansion corresponding to state ψ_i and atomic orbitals ϕ_m. N denotes the total number of orbital bases used or the size of the Hamiltonian. Elements of the tight-binding $H^{\rm tb}$ are of the two-center Slater-Koster [45] form,

$$H^{\rm tb}_{mn} = \int \phi^*_m(r)\left(\frac{-\nabla^2}{2} + V(r - R_A) + V(r - R_B)\right)\phi_n(r)d^3r, \tag{3}$$

where m and n denote orbital indices, A and B denote atoms, and $\phi_m(r)$ and $\phi_n(r)$ denote the respective atomic orbitals. Orthogonality of the basis set, $\langle\phi_m|\phi_n\rangle = \delta_{mn}$, is assumed. Electronic structure is computed only at the $\Gamma-$point in reciprocal space. Thus, the electronic structure of the system can be obtained by solving the eigensystem,

$$H^0\vec{c}_i = E_i\vec{c}_i, \tag{4}$$

where E_i and $\vec{c}_i$ denote the energies and linear expansion coefficients of the single-particle eigenstates ψ_i, respectively. The lowest $\frac{N_{\rm el}}{2}$ of these eigenstates are assumed to be occupied, where $N_{\rm el}$ denotes the number of electrons, and 2 accounts for spin degeneracy.

In the presence of a driving external voltage, the electrostatic potential is assumed to have a linear spatial profile, so that the external potential shifts energies on the left and right dielectric states by $eV_{\rm left}$, and $eV_{\rm right}$, respectively, and shifts the energy of the argon atoms by $\mathrm{eV}(R_{\rm Ar})$. ac and dc Stark shift of atomic states [46], and other modifications of energy levels are not considered. In the atomic basis, the resulting Hamiltonian is

$$H^{\rm total} = H^0 + ef(t)\begin{bmatrix} V_{\rm left} & 0 & 0 \\ 0 & V(R_{\rm Ar}) & 0 \\ 0 & 0 & V_{\rm right} \end{bmatrix}, \tag{5}$$

where $f(t)$ takes the time-dependent nature of the potential difference into account, and e accounts for electronic charge.

C. Adiabatic approximation

Assuming the time-dependent part of the external voltage, $f(t)$, to be infinitely slow, the adiabatic approximation is used to compute the rate of electron transfer at the simplest level. The instantaneous eigenstates of the time-dependent Hamiltonian, $H^{\rm total}$ of Eq. (5), the ground-state density matrix, $\mathbf{P}(t)$, and the charge density on the left dielectric, $n_{\rm left}(t)$, are computed according to

$$\left(H^0 + ef(t)\begin{bmatrix} V_{\rm left} & 0 & 0 \\ 0 & V(R_{\rm Ar}) & 0 \\ 0 & 0 & V_{\rm right} \end{bmatrix}\right)\vec{c}_i(t) = \epsilon_i\vec{c}_i(t),$$

$$\mathbf{P}(t) = \sum_{i=1}^{N_{el}/2}\vec{c}_i(t)\vec{c}_i^{\,\rm T}(t),$$

$$n_{\rm left}(t) = \sum_{\alpha\in{\rm left}}\mathbf{P}(t)_{\alpha,\alpha}, \tag{6}$$

where $\vec{c}_i(t)$ and $\vec{c}_i^{\,\rm T}(t)$ denote the ith eigenvector and eigenvector-transpose of the total Hamiltonian at time t. The number of electrons on the left and right dielectric layers, as well as the argon region, are obtained by taking partial traces of the density matrix. The change in total charge (and corresponding effective current) on the left dielectric surface is computed from

$$I(t) = \frac{\Delta n_{\rm left}}{\Delta t} \approx \frac{n(t + \Delta t) - n(t - \Delta t)}{2\Delta t}. \tag{7}$$

D. Theory of nonadiabatic transitions

Next, the theory of nonadiabatic transitions [24–26,30,47] is used to compute the rate of electron transfer under a time-dependent external voltage. The eigenstates of the zero-field Hamiltonian in Eq. (4) are used as the diabatic states, and a sinusoidal potential with frequency of 20 kHz is used for time-dependence. In the simplest two-state form, eigenvectors of a time-independent 2×2 Hamiltonian $\hat{h}^0$ can be computed and labeled $|1\rangle$ and $|2\rangle$, with energies E_1 and E_2. If a time-dependent shift $\pm\frac{F(t)}{2}$ is applied to these eigenstates such that

$$\epsilon_1(t) = E_1 + \frac{F(t)}{2}, \tag{8a}$$

$$\epsilon_2(t) = E_2 - \frac{F(t)}{2}, \tag{8b}$$

then the time-dependent diabatic energies $\epsilon_1(t)$ and $\epsilon_2(t)$ can cross at time t_{12} as observed in Fig. 4, where the diabatic energy levels $\epsilon_1(t)$ and $\epsilon_2(t)$ are represented by dashed lines that are expected to cross at time t_{12}. The solid lines of Fig. 4 present the actual time-dependent energy-levels of the interacting, time-dependent Hamiltonian, where level crossing is avoided due to the interaction between single-particle states, V_{12}. Moving from left to right in Fig. 4, the solid lines show the adiabatic evolution of the system in the infinitely slow limit: $|1\rangle \to |2'\rangle$ and $|2\rangle \to |1'\rangle$. The dashed lines show diabatic evolution of the system in the infinitely fast limit: $|1\rangle \to |1'\rangle$, and $|2\rangle \to |2'\rangle$.

The dynamics of time-evolution depend on the coupling strength, V_{12}, and the slew rate defined as the rate of variation of the time-dependent Hamiltonian, $\frac{\partial F(t)}{\partial t}$, via the dimensionless ratio [30]:

$$\Gamma = \frac{|V_{12}|^2}{\hbar\left|\frac{\partial F(t)}{\partial t}\right|} = \left|\frac{e^2}{4\pi\epsilon_0 r_{12}}\right|^2\frac{1}{\hbar|\omega eV_0\cos\omega t|}, \tag{9}$$

where e denotes electronic charge, and ϵ_0 is the dielectric constant. The slew rate, $\frac{\partial F(t)}{\partial t}$, is computed at the expected

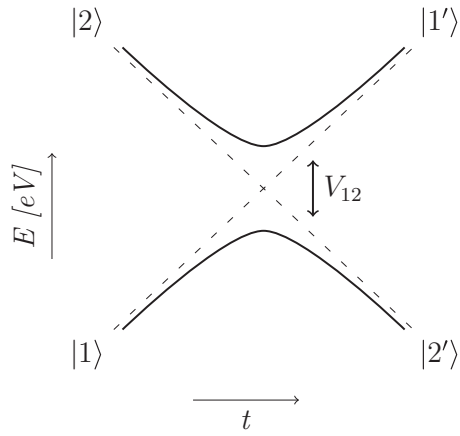

FIG. 4. Energy-level crossing of two states due to a time-dependent parameter. $|1\rangle$ and $|2\rangle$ denote diabatic states, and their energy levels are represented by dashed lines that are expected to cross at time t_{12}. Direct intersection, or level crossing, is avoided when a coupling term, V_{12}, exists. If the time-dependent parameter is varied sufficiently slowly, the system undergoes adiabatic transitions given by $|1\rangle \to |2'\rangle$, and $|2\rangle \to |1'\rangle$.

level crossing of diabatic energy levels (t_{12}), and the interstate coupling $V_{12} = \frac{1}{|r_1 - r_2|} = \frac{1}{r_{12}}$, is used.

In the limit $t_{\text{initial}} = -\infty$ and $t_{\text{final}} = +\infty$, and assuming $F(t)$ is linear near the energy-level crossing, the probability of diabatic transitions is given by [30]

$$D = P_{|1\rangle\to|1'\rangle} = P_{|2\rangle\to|2'\rangle} = e^{-2\pi\Gamma} \tag{10a}$$

and the probability for adiabatic transition is computed according to

$$A = P_{|1\rangle\to|2'\rangle} = P_{|2\rangle\to|1'\rangle} = 1 - D = 1 - e^{-2\pi\Gamma}. \tag{10b}$$

E. Generalization to multiple states

Figure 5 shows one example of generalization of level crossing to systems with multiple states: The system consists of six diabatic states and their level crossings, with

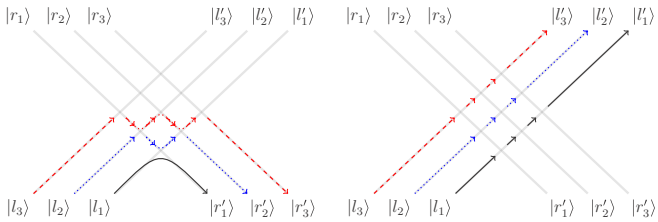

(a) All adiabatic transitions (b) All diabatic transitions

FIG. 5. Generalization of the two-state level-crossing problem to multistate level crossing, with six diabatic states: three localized on the left and denoted by $|l_1\rangle, |l_2\rangle, |l_3\rangle$, and three on the right denoted by $|r_1\rangle, |r_2\rangle, |r_3\rangle$. Initially, the three states on the left are occupied. (a) The system evolves fully adiabatically, leading to the system evolution $\{|l_1\rangle, |l_2\rangle, |l_3\rangle\} \to \{|r'_1\rangle, |r'_2\rangle, |r'_3\rangle\}$. All electrons on the left and transferred to the states localized on the right. (b) All transitions are diabatic, leading to the system evolution $\{|l_1\rangle, |l_2\rangle, |l_3\rangle\} \to \{|l'_1\rangle, |l'_2\rangle, |l'_3\rangle\}$, with no electrons transferred.

three states localized on the left $|l_1\rangle, |l_2\rangle, |l_3\rangle$, and three on the right $|r_1\rangle, |r_2\rangle, |r_3\rangle$. Solid straight lines show the diabatic energy levels under an external potential. In Fig. 5(a), all transitions are adiabatic and electrons previously on the left are transferred to states on the right, $\{|l_1\rangle, |l_2\rangle, |l_3\rangle\} \to \{|r'_1\rangle, |r'_2\rangle, |r'_3\rangle\}$. On the other hand, Fig. 5(b) shows the evolution of the system when all transitions are diabatic, resulting in no electron transfer as $\{|l_1\rangle, |l_2\rangle, |l_3\rangle\} \to \{|l'_1\rangle, |l'_2\rangle, |l'_3\rangle\}$. The exact computation of the density matrix (or many-electron wave function) and integration over long timescales is an active area of investigation, under various limiting conditions [31,48–55].

In this paper, the Landau-Zener problem is generalized to multiple states in the incoherent limit [31], where interference effects between two level-crossing events are ignored. This is a semiclassical approximation where a superposition of states is replaced by a classical ensemble of trajectories, so that time-evolution is modeled as a series of independent level crossings. While not exact, it can be justified by observing that the ac voltage has frequencies of ∼kHz while oscillations of electronic states correspond to frequencies of ∼THz. Even in the semiclassical limit, however, the number of possible paths scales exponentially with the number of level crossings, and instead of computing a distribution of all possible trajectories, the ensemble average is used. Thus, our computation can be summarized as follows: First, the times for all possible level-crossing events are obtained by setting $\epsilon_i(t_{ij}) = \epsilon_j(t_{ij})$, and are time-ordered. Then, at each t_{ij}, the occupation of states, $[f_i^0, f_j^0]^T$, is updated according to the following equation:

$$\begin{bmatrix} f_i \\ f_j \end{bmatrix} = \begin{bmatrix} D & A \\ A & D \end{bmatrix} \begin{bmatrix} f_i^0 \\ f_j^0 \end{bmatrix}. \tag{11}$$

Finally, random atomic motion is ignored, although the effects of dissipation and temperature have been investigated in other systems [48,56]. The interplay between finite temperature and dissipation may result in nonmonotonic deviations from the idealized Landau-Zener case [56]. In our case, however, the gaseous region itself may undergo plasma formation, so that more consideration is necessary to define a heat bath appropriately. As such, the effects of temperature and dissipation are important but beyond the scope of this paper.

III. RESULTS

In this section, we present the density of states of $\alpha-$quartz, along with the effects of surface termination and hydrogenation. The shift in the density of states of two dielectric regions separated by an external voltage is also presented. Next, we present the rates of electron transfer, assuming that the dielectric-gas-dielectric system evolves adiabatically and reversibly in the infinitely slow limit. The time-dependent variation of diabatic energy levels under a finite ac voltage is then investigated in Sec. III C. Finally, the evolution of the dielectric-gas-dielectric system is computed within the theory of nonadiabatic transitions, and Secs. III D–III F present the rates of electron transfer as well as charge accumulation or depletion from the dielectric layer of interest under a variety of operating conditions.

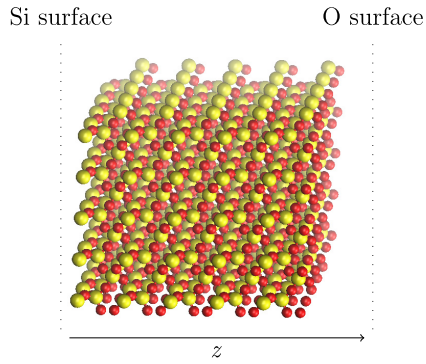

(a) Unit cell of α-quartz with 0001 termination.

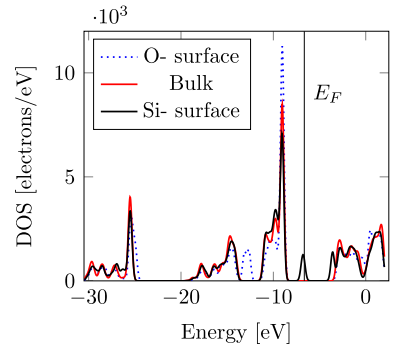

(b) Projected density of states of the unit cell on the left.

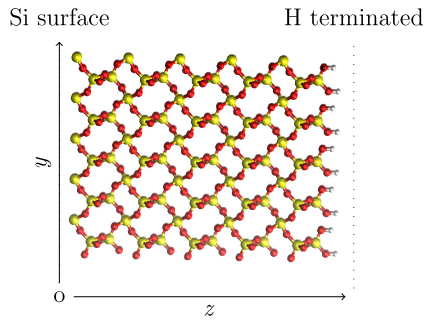

(c) -OH terminated surface.

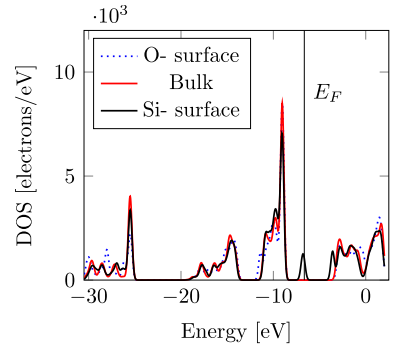

(d) Density of states after hydrogen termination.

FIG. 6. Appearance of surface states due to termination of bulk α-quartz along the 0001 direction. (a) The unit cell has periodic boundary conditions in the x and y directions, while along the z direction, the surface is terminated. (b) The projected density of states in the bulk, Si-exposed, and O-exposed surfaces, show features consistent with surface states. (c) The surface of interest in this work has exposed oxygen atoms bonded to hydrogen, leading to a less reactive, −OH terminated surface. (d) The resulting density of states of the system shows the effect of H termination.

A. Density of states of the $\alpha-$quartz surface

Figure 6 presents the density of states of $\alpha-$quartz terminated along the 0001 direction (z direction), with periodic boundary conditions in the x and y directions. The unit cell, shown in Fig. 6(a), consists of $5 \times 5 \times 5$ nine atom primitive unit cells of $\alpha-$quartz, with corresponding density of states shown in Fig. 6(b). The band gap obtained is ∼6.3 eV, which is within the range of values reported in the literature [57–59]. In addition to the bulk density of states, Fig. 6(b) also shows the projected density of states on the exposed atomic layers, where we note the appearance of surface states due to the O-terminated surface and the Si-terminated surface, at different parts of the energy spectrum. E_F denotes the highest energy level occupied at zero temperature. The surface states in the O-terminated region are below E_F, and are expected to be occupied, indicating surface charge. The Si-terminated surface is assumed to be far away from the gaseous region, and expected to connect to metallic electrodes.

Figure 6(c) shows the dielectric layer after the O-terminated surface has been stabilized by hydrogenation. Here, we have assumed that every dangling O bond absorbs a hydrogen atom to form an −OH terminated surface. The effect of −OH termination is then observed in the density of states, shown in Fig. 6(d), where the presence of hydrogen coverage has changed the density of states of the −OH surface such that the effect of surface termination is not concentrated in one region of the energy spectrum. This hydrogen-covered 0001 surface interfaces with the gaseous regions in our simulations.

Figure 7 presents an intuitive picture of the ground state of the system in the presence of a potential difference between the left and right walls: Energies of the left and right are relatively shifted due to the potential difference. If the number of electrons is conserved, and the system is allowed to relax to the ground state, the charge distribution between the left and right walls is unequal. Under a slow (allowing for the system to relax to the ground state) but time-dependent potential difference, the number of electrons on the left and right dielectrics varies with time, with electrons being transferred between the two regions at different times.

B. Adiabatic approximation

The results of Sec. III A suggest that time-dependent electron transfer could be quantified from the occupation of electronic states at the instantaneous ground states. Figure 8 shows the results of that computation, where the instantaneous

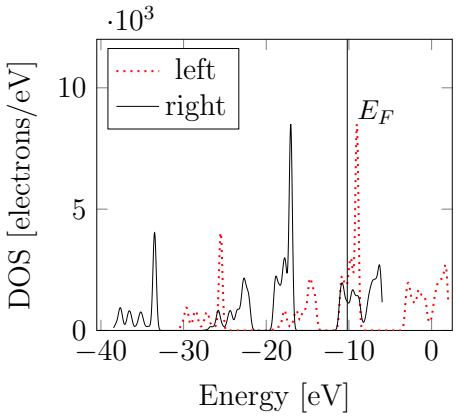

FIG. 7. Expected shift in energies of the left and right dielectric layers due to the external potential difference. In case of a time-dependent potential difference, the instantaneous ground state of the system results in different occupations of states localized on the left and right dielectrics, indicating the possibility of time-dependent electron transfer.

ground-state density matrix of the time-dependent Hamiltonian is computed; the time-dependent nature of electron transfer is evident in the phase lag between the observed current $I(t)$, and applied voltage $V(t)$. A sinusoidal potential difference with $V_0 = E_{\max} d_{\text{gap}}$ is applied, with a fixed maximum electric field, $E_{\max} = 1.04 \times 10^6$ V/cm, to avoid the effects of dielectric breakdown in microgaps. In addition to the temporal profile of current and voltage, a first-order approximation of the electrostatic potential is also plotted in Figs. 8(a)–8(d), where (a) and (d) denote two points near zero field in the ac cycle. Localized regions of variation in electrostatic potential in Fig. 8(b) denote electron transfer from the left dielectric surface into the argon region, while Fig. 8(c) shows the electrostatic potential as the electrons are transported to the right dielectric. Despite the simplicity of the model, the spatial profile of $V(r)$ obtained is qualitatively similar to the expected electric potential [cf. Fig. 2(a)].

C. Diabatic energy levels under time-dependent $V(t)$

Next, Fig. 9 shows the variation of diabatic energy levels under ac voltage, with the frequency set to 20 kHz. First, Figs. 9(a) and 9(b) show the variation of diabatic energy levels of the left and right dielectric layers, absent intermediate argon atoms, for $V_0 = 20$ V and $V_0 = 20$ kV respectively. In the case of $V_0 = 20$ V, diabatic energy levels of states on the left and right intersect at a wide range of times, while for $V_0 = 20$ kV, all level-crossings appear concentrated near the half cycles. Next, Fig. 9(c) shows the diabatic energy levels of the system, now with intermediate argon atoms: The dielectric layers are separated by $d_{\text{gap}} = 1$ cm, and the number of argon atoms is determined by using the ideal gas law at pressure $P = 20$ Pa and temperature $T = 300$ K. An external sinusoidal ac voltage with $V_0 = 400$ V is applied. The argon atoms are placed at random within the gap, and assumed to be stationary, with each atom contributing 14 orbitals. As a result, while the diabatic states on the left and right dielectric layers vary sinusoidally with opposing slopes $\frac{\partial E(t)}{\partial t}$, additional discrete energy levels can be found in the

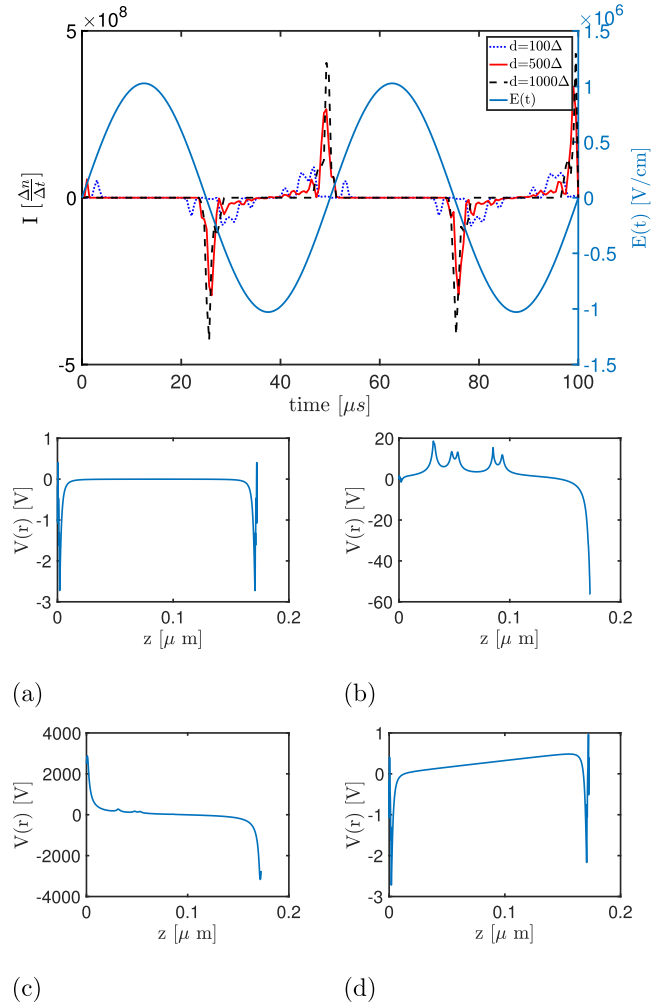

FIG. 8. Results of electronic-structure calculations in the adiabatic limit. The topmost panel shows the effective rates of electron transfer obtained from direct computation of instantaneous ground state of the time-dependent Hamiltonian, where $\Delta \approx 17$ Å, the thickness of the atomistic dielectric layer. Next, for the case of $d_{\text{gap}} = 100\Delta$, subfigures (a)–(d) show the spatial profile of the electrostatic potential at various points in the ac cycle, at phases corresponding to $\{0, \frac{6\pi}{100}, \frac{\pi}{2}, \pi\}$. (a) and (d) correspond to the beginning and end of the half cycle near zero field, while in (b), localized regions with high electric field indicate the presence of additional electrons in the gaseous region. In (c), the electrostatic potential is in agreement with the expected spatial profile during plasma formation in Fig. 2(a).

energetic gap between energies of the left and right dielectric layers. Figure 9(c) suggests that the presence of argon atoms increases the number of, and broadens the times at which level crossings (and electron transfer) can occur.

D. Electron transfer at constant maximum electric field

Given the time-dependent diabatic energy levels of the previous section, the probabilities of diabatic and adiabatic transitions, and the rates of electron transfer can be computed. This section presents the rates of electron transfer when the maximum electric field V_0/d_{gap} is held constant, to 1.04×10^6 V/cm, for various gap distances; the frequency of

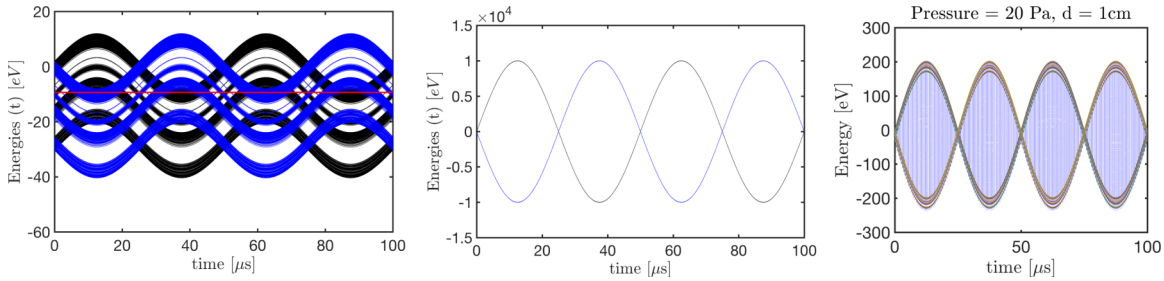

(a) $V_0 = 20\,V$, vacuum (b) $V_0 = 20\,kV$, vacuum (c) $V_0 = 400V$, $20\,Pa$

FIG. 9. Diabatic energy-level crossings under ac voltages at frequency, $f = 20$ kHz. (a) Diabatic energy levels of states localized on the left and right dielectric layers under ac voltage corresponding to $V_0 = 20$ V. (b) Diabatic energy levels under $V_0 = 20$ kV. (c) $V_0 = 400$ V, and with intermediate argon atoms between dielectric surfaces. Comparing (a) and (b), note that level crossings occur at a broad range of times under lower voltage $V_0 = 20$ V, while under $V_0 = 20$ kV, all level-crossings occur near half-cycles of $V(t)$. In (c), the presence of intermediate argon atoms increases the number of level crossings as well as broadens the times at which level crossings, and corresponding electron transfer, can occur.

ac voltage is set to 20 kHz. Electron transfer is computed, both for vacuum separation between dielectric surfaces, and in the presence of a fixed number of intermediate argon atoms, $N_{ar} = 180$.

Figures 10(a)–10(c) present the results of our computation, where gap distances are set to (a) $d_{gap} = 10\ \mu$m, (b) $d_{gap} = 100\ \mu$m, and (c) $d_{gap} = 1$ cm. In each plot, electron emission is presented in the case of vacuum separation ($\times 10$ for visibility) and in the presence of intermediate argon atoms. Assuming $T = 300$ K and using the ideal gas law, $N_{ar} = 180$ atoms in the intermediate region correspond to pressures of (a) 1.01×10^4 Pa, (b) 1.01×10^3 Pa, and (c) 10.1 Pa. Since the maximum electric field, V_0/d_{gap}, is held fixed, increase in the gap distance also corresponds to voltages of (a) $V_0 = 1.04 \times 10^4$ V, (b) $V_0 = 1.04 \times 10^3$ V, and (c) $V_0 = 1.04 \times 10^6$ V. In each plot, the left y axis presents the rate of electron transfer from the left dielectric, Δn_L, while the right y axis presents the applied ac voltage. Comparing the magnitudes of electron emission (scales in the left y axes) in different plots of Fig. 10, we note that increase in the gap distance decreases the rate of electron transfer—this is because increase in the distance between diabatic states, r_{12}, in general leads to lower probabilities of adiabatic transitions (and corresponding electron transfer). Importantly, we note in Fig. 10(c), that for a gap distance of 1 cm and vacuum separation, electron transfer is negligible despite the large ac voltage, $V(t)$, applied.

In addition, scaling of $\times 10$ used to plot electron emission under vacuum separation in Fig. 10 indicates that the presence of intermediate argon atoms increases the rate of electron emission for all operating conditions that were investigated. Intermediate argon atoms not only lead to additional level-crossing events, but these level crossings also correspond to shorter distances between diabatic states, r_{12}, which are favorable to adiabatic transitions (and electron transfer). Thus,

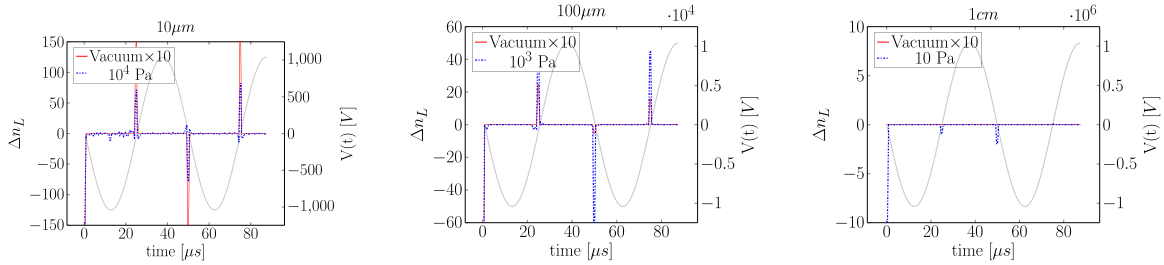

(a) $V_0 = 1.04 \times 10^3\,V$ (b) $V_0 = 1.04 \times 10^4\,V$ (c) $V_0 = 1.04 \times 10^6\,V$

FIG. 10. Time-dependent electron transfer between dielectric surfaces under fixed V_0/d_{gap}, as the gap distance, d_{gap}, is set to (a) 10 μm, (b) 100 μm, and (c) 1 cm, with corresponding change in the ac voltage, $V(t)$, on the right y axis of each plot. On the left y axis, Δn_L denotes the rate of electron transfer from the left dielectric. In each plot, the rates of electron emission are presented in the case of vacuum separation, and in the presence of a fixed number of intermediate argon atoms, which corresponds to pressures of (a) 10^4 Pa, (b) 10^3 Pa, and (c) 10 Pa, respectively. The rate of electron transfer in case of vacuum separation is multiplied by a factor of ($\times 10$) for comparison. Comparing the magnitudes of electron transfer for various gap distances in different plots, we note that as the gap distance is increased, the magnitudes of Δn_L decreases, as the distance between diabatic states, r_{12}, adversely affects the probability of adiabatic transition (and corresponding electron transfer). In particular, when (c) $d_{gap} = 1$ cm, and under vacuum separation, electron transfer is negligible despite large values of $V(t)$. Second, the presence of intermediate argon atoms increases the rate of electron transfer; this is because intermediate argon atoms not only lead to additional level crossings, but these level crossings also correspond to smaller distances between diabatic states, r_{12}, leading to an overall increase in electron emission. Finally, we note that electron emission from surface walls is a necessary but insufficient condition for plasma formation. As such, the computed temporal profiles of electron transfer are consistent with, and provide partial predictions for, the observed temporal profiles of plasma formation in the literature [32–35].

the overall effect of the presence of intermediate argon atoms is a consistent increase in the rate of electron emission, for a variety of operating conditions.

Finally, we note that the temporal profiles of electron emission computed in this section are qualitatively consistent with the observed temporal profiles of plasma formation reported in the literature [32–35]. We have shown that electron transfer from the dielectric to the argon region under an ac voltage is time dependent, and that the dielectric region can provide electrons for plasma generation. Although electric fields in microscale plasmas can approach values around 10^6 V/cm, the operating conditions for plasma devices are provided in terms of the applied voltage regardless of the gap distance, and are in the kV range [7]. Therefore, the next section investigates electron transfer when the ac voltage and gap distance are varied separately.

E. Electron transfer at constant maximum voltage

In this section, we investigate the rates of electron transfer when the external voltage and gap distance are varied independently. In particular, ac voltages corresponding to $V_0 = \{40\text{ V}, 4000\text{ V}\}$ and gap distances $d_{\text{gap}} = \{1\ \mu\text{m}, 1\text{ cm}\}$ are investigated with and without intermediate argon atoms. Figure 11 presents the results of our computation. The first column, Fig. 11(a), and the second column, Fig. 11(b), present results for $V_0 = 40$ V and $V_0 = 4000$ V, respectively, while the first and second rows of Fig. 11 represent configurations with $d_{\text{gap}} = 1\ \mu$m and $d_{\text{gap}} = 1$ cm, respectively. The magnitudes and temporal profiles of electron transfer under ac voltage of $V_0 = 4000$ V agree with experimental profiles [32–35], as well as conclusions of the previous section.

However, reducing the ac voltage to $V_0 = 40$ V, in Fig. 11(a), appears to have two effects. First, in the case of vacuum separation, the temporal profile of electron transfer is broader under $V_0 = 40$ V than under $V_0 = 4000$ V. This is consistent with our discussion in Sec. III C, where it was observed that level-crossing events are more broadly distributed in time for smaller V_0. Second, in the presence of intermediate argon atoms, electron transfers also occur near the maximum value of $V(t) = V_0$. Since electron transfer to the gaseous region is a necessary but insufficient condition for plasma generation, this qualitative change in time-dependent electron emission provides a partial microscopic explanation for the

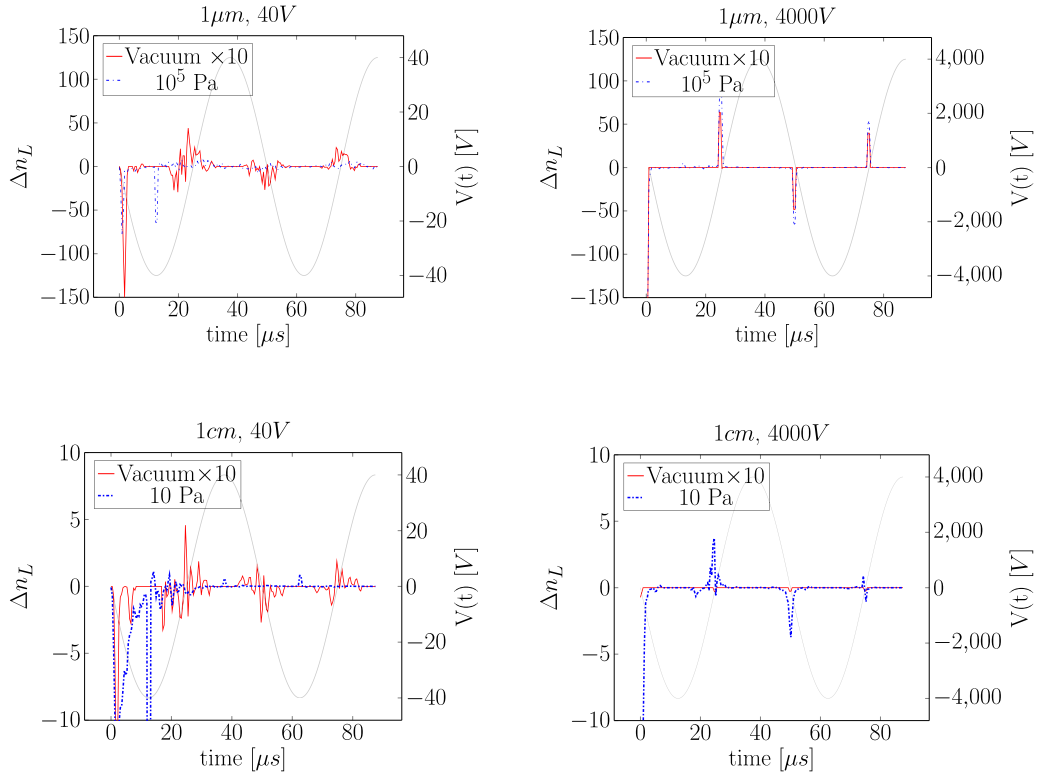

(a) $V_0 = 40\,V$ (b) $V_0 = 4000\,V$

FIG. 11. Electron transfer for gap distances of 1 μm (first row) and 1 cm (second row), under ac voltages (a) $V_0 = 40$ V and (b) $V_0 = 4000$ V. As expected, electron transfer is negligible for vacuum separation when $d_{\text{gap}} = 1$ cm, while the presence of intermediate argon atoms increases the rate of electron transfer. In agreement with results of the previous section, electron transfer for $d_{\text{gap}} = 1\ \mu$m (first row) is greater than that for $d_{\text{gap}} = 1$ cm (second row), due to the effect of distance between diabatic states, r_{12}, on the probability of adiabatic transition. Comparing the temporal profiles of (a) and (b), we note that for $V_0 = 40$ V and vacuum separation, the temporal profile of electron emission is broadened. More importantly, we observe in (a) that under $V_0 = 40$ V and in the presence of intermediate argon atoms ($P = 10^5$ Pa and $P = 10$ Pa), the temporal profile of electron emission undergoes a qualitative shift, resulting in significant electron transfers near the maximum $V(t)$. This behavior provides a partial microscopic explanation to experimental observations of delayed plasma formation when the ac voltage is lowered [60, cf. Figs. 5 and 13 therein].

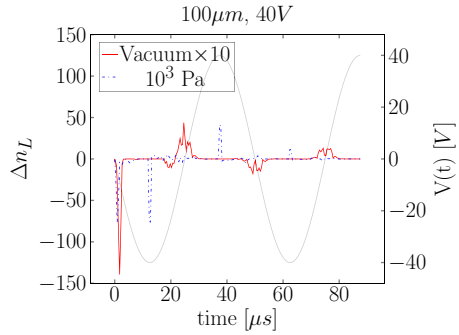

FIG. 12. Qualitative change in the time dependence of electron emission at low ac voltage with intermediate argon atoms present. Under high voltages ($V_0 = 4000$ V) or under vacuum separation, the temporal profile of electron emission is similar to the vacuum case (solid red line). However, when the ac voltage is lowered and intermediate argon atoms are present, the temporal profile of electron emission shifts (dashed blue line). This observation is consistent with, and provides a partial explanation for, experimentally observed delay in plasma formation under reduced ac voltage [60, cf. Figs. 5 and 13 therein].

observation that decreasing the maximum ac voltage also delays breakdown [60, cf. Figs. 5 and 13 therein]. This qualitative shift in the temporal behavior of electron emission is more pronounced in the intermediate case of $d_{\text{gap}} = 100$ μm, $P = 10^3$ Pa for $V_0 = 40$ V, shown in Fig. 12.

The results of this subsection demonstrate that both the magnitudes and time-dependence of electron transfer are affected by a combination of gaseous pressure, ac voltage, and gap distance between dielectric surfaces. The magnitude of the ac voltage, V_0, can change the temporal profile of electron transfer by changing the times at which energy-level crossings occur; the number of intermediate argon atoms can also change the number of energy-level crossings, and also lead to higher probabilities of electron transfer, due to the decreased distance between diabatic states, r_{12}. Although underexplored in this paper, the probability of electron transfer at level crossing is also affected by the magnitude and frequency of ac voltage via the slew term, $\frac{\partial V(t)}{\partial t}$. We anticipate future studies that explore the parameter space consisting of pressure, operating voltage, and gap distance, and their effects on electron transfer from dielectric surfaces.

F. $Q - V$ profile or Lissajous plots

Results of the previous subsections showed the effect of the applied voltage, gap distance, and ambient pressure on the magnitude and temporal profile of electron transfer. Next, we consider a single gap distance of $d_{\text{gap}} = 100$ μm, and look at charge accumulation and charge depletion, and the corresponding Lissajous plots in Fig. 13. Of the computationally feasible systems considered in this paper so far, the system with $d_{\text{gap}} = 100$ μm, $N_{\text{atoms}} = 180$, and $V_0 = 4000$ V is closest to the general operating conditions of symmetric DBDs in terms of the pressure, gap distance, and ac voltage between dielectric surfaces.[7]

Figure 13(a) presents the rate of electron transfer from the left dielectric layer, while Fig. 13(b) shows the total charge on the left dielectric as a function of time. Peaks in electron

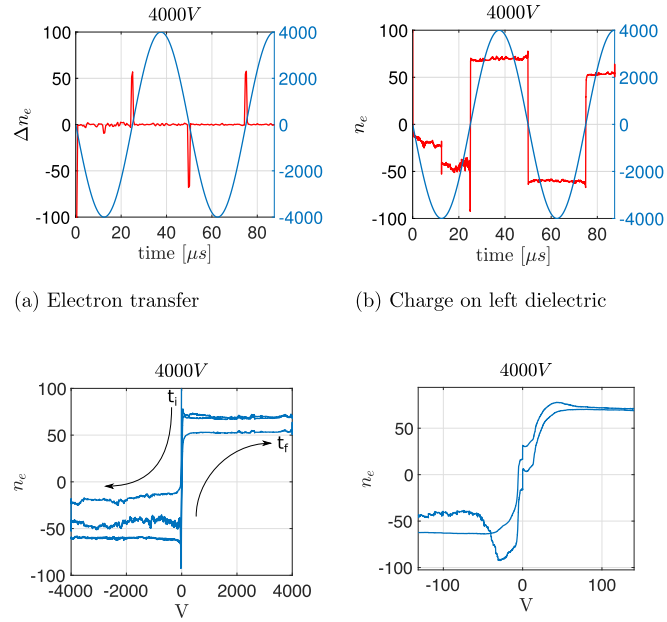

(a) Electron transfer

(b) Charge on left dielectric

(c) Lissajous plot of charge-vs-voltage

(d) Lissajous plot of one AC cycle near 0 V

FIG. 13. (a) The temporal profile of electron transfer for $d_{\text{gap}} = 100$ μm and $P = 1.01 \times 10^3$ Pa (b) The total charge on the left dielectric as a function of time, $n_e(t)$, on the left y axis, with the ac voltage $V(t)$ on the right y axis. (c) The corresponding Lissajous plot obtained by using $(x, y) = [V(t), n_e(t)]$, where t_i and t_f denote the initial and final times of the simulation. (d) Zoomed-in Lissajous plot showing one complete ac cycle between the phases $\{\frac{\pi}{2}, 2\pi + \frac{\pi}{2}\}$. Note the scales on the x and y axes due to the zoom-in.

transfer in Fig. 13(a) correspond to sudden transitions in the number of electrons in Fig. 13(b). Figure 13(b) shows the depletion and accumulation of electrons on the dielectric layer; measurements of surface charge [61,62] qualitatively agree with our results. Figure 13(c) presents the corresponding Lissajous plot showing instantaneous charge vs voltage on the left dielectric. First, we note that if the time evolution of the system were reversible (e.g., if all transitions were adiabatic), the values of $n_e(t)$ would overlap for the same $V(t)$. Figure 13(d) presents the Lissajous plot corresponding to a single ac cycle, zoomed in to show the convex area in the Lissajous plot.

Compared to experimental measurements [35,62], we note two key differences made evident by the Lissajous plots in Figs. 13(c) and 13(d). First, in general, the area inside a Lissajous plot is associated with energy consumption due to various irreversible processes—electron transfer between dielectric and gaseous regions, electron-impact ionization and plasma formation, as well as heat loss due to the motion of atoms. The area inside the computed Lissajous plots shown in Figs. 13(c) and 13(d), is underestimated because this present paper does not include the dissipative effects of electron-impact ionizations, atomic motion, and plasma evolution. In addition, inclusion of a macroscopic dielectric layer would allow us to incorporate the effects of a voltage drop and energy dissipation in the dielectric system, increasing the magnitude of the threshold $V(t)$ at which the Lissajous plot in Fig. 13(d)

opens to convexity. Second, in Fig. 13(c), horizontal lines away from the transition region denote near constant charge n_e for varying voltage or near-zero capacitance. A more expensive but accurate self-consistent charge tight-binding calculation, and measurement of surface charge on a predetermined surface instead of a volumetric integral over a thin dielectric slab as in the present paper, can improve these results.

IV. CONCLUSION AND FUTURE WORK

In this paper, we present a time-dependent model of electron emission from dielectric surfaces under ac voltage that is based on electronic structure theory and dynamical level crossing. This model is motivated by the necessity of predicting electron emission from dielectric surfaces in DBD plasma generators; as such, it predicts time-dependent electron emission that is qualitatively consistent with the observed temporal profile of plasma formation reported in the literature [32–35]. Previously, the time-dependence of experimentally measured current in DBDs was explained primarily via a circuit model containing resistive and capacitive elements, and a switch controlling plasma formation. At the microscopic level, gaseous breakdown could be modeled as an avalanche of electron-impact ionization events—electron emission from dielectric surface walls was assumed, but a theoretical model was missing.

A semiempirical tight-binding parametrization for a thin layer of dielectric $\alpha-$quartz, and a quasiparticle, occupation-based model for argon atoms are used to investigate the charge transfer mechanism. Exact time-integration of the density matrix over timescales in the microseconds regime remains computationally infeasible, and charge transfer is modeled in the incoherent limit of the multistate Landau-Zener problem, as a series of independent level crossings. We find that both the magnitude and time-dependence of electron emission vary as a function of the gaseous pressure, applied voltage, and gap distance between dielectric surfaces. The computation and tabulation of time-dependent coefficients of electron emission under various operating conditions will be a direct extension of this paper, eventually allowing for the integration of these surface-based initial and boundary conditions with plasma simulations [15,16,63].

Random atomic motion in the gaseous region is set to zero, and future work is necessary to incorporate the effects of temperature and dissipation [48,56]. Within DBD devices, temperature and dissipation not only affect the rate of electron transfer, but also contribute to plasma formation in the gaseous region. Thus, more work is necessary to appropriately couple a heat bath with the possibility of a phase transition, and will be considered in the future.

ACKNOWLEDGMENTS

Discussions with Jon Retter, Kyle Mackay, Kelly Stephani, Munetake Nishihara, Luca Massa, as well as other members of XPACC are gratefully acknowledged. This material is based [in part] upon work supported by the Department of Energy, National Nuclear Security Administration, under Award No. DE-NA0002374.

[1] W. Siemens, Ueber die elektrostatische induction und die verzögerung des stroms in flaschendrähten, Ann. Phys. **178**, 66 (1857).

[2] G. Borcia, C. Anderson, and N. Brown, Dielectric barrier discharge for surface treatment: Application to selected polymers in film and fibre form, Plasma Sources Sci. Technol. **12**, 335 (2003).

[3] J. Retter, G. Elliott, and S. Kearney, Dielectric-barrier-discharge plasma-assisted hydrogen diffusion flame. Part 1: Temperature, oxygen, and fuel measurements by one-dimensional fs/ps rotational CARS imaging, Combust. Flame **191**, 527 (2018).

[4] H. Wagner, R. Brandenburg, K. Kozlov, A. Sonnenfeld, P. Michel, and J. Behnke, The barrier discharge: Basic properties and applications to surface treatment, Vacuum **71**, 417 (2003).

[5] B. Eliasson, M. Hirth, and U. Kogelschatz, Ozone synthesis from oxygen in dielectric barrier discharges, J. Phys. D **20**, 1421 (1987).

[6] U. Kogelschatz, B. Eliasson, and W. Egli, From ozone generators to flat television screens: History and future potential of dielectric-barrier discharges, Pure Appl. Chem. **71**, 1819 (1999).

[7] R. Brandenburg, Dielectric barrier discharges: Progress on plasma sources and on the understanding of regimes and single filaments, Plasma Sources Sci. Technol. **26**, 053001 (2017).

[8] Y. Raizer and J. Allen, *Gas Discharge Physics*, Vol. 2 (Springer, Berlin, 1997).

[9] A. Loveless and A. Garner, Scaling laws for gas breakdown for nanoscale to microscale gaps at atmospheric pressure, Appl. Phys. Lett. **108**, 234103 (2016).

[10] A. Semnani, A. Venkattraman, A. Alexeenko, and D. Peroulis, Frequency response of atmospheric pressure gas breakdown in micro/nanogaps, Appl. Phys. Lett. **103**, 063102 (2013).

[11] M. Stengel and N. A. Spaldin, *Ab initio* theory of metal-insulator interfaces in a finite electric field, Phys. Rev. B **75**, 205121 (2007).

[12] G. Bordier and C. Noguera, Electronic structure of a metal-insulator interface: Towards a theory of nonreactive adhesion, Phys. Rev. B **44**, 6361 (1991).

[13] A. Okiji, H. Kasai, and S. Terakawa, Electronic states near metal-insulator interface, J. Phys. Soc. Jpn. **44**, 1275 (1978).

[14] P. Bletzinger and B. Ganguly, The effect of displacement current on fast-pulsed dielectric barrier discharges, J. Phys. D **36**, 1550 (2003).

[15] G. Bird, Molecular gas dynamics, NASA STI/Recon Technical Report A **76** (1976).

[16] C. Munz, M. Auweter-Kurtz, S. Fasoulas, A. Mirza, P. Ortwein, M. Pfeiffer, and T. Stindl, Coupled particle-in-cell and direct simulation Monte Carlo method for simulating reactive plasma flows, C. R. Méc. **342**, 662 (2014).

[17] W. Fan, Z. Sheng, L. Dong, F. Liu, X. Zhong, Y. Cui, F. Hao, and T. Du, Formation of side discharges in dielectric barrier discharge, Sci. Rep. **7**, 8368 (2017).
[18] S. Tholeti, G. Shivkumar, and A. Alexeenko, Field emission microplasma actuation for microchannel flows, J. Phys. D **49**, 215203 (2016).
[19] K. K. Mackay, J. B. Freund, and H. T. Johnson, Enhancement of hydrogen microcombustion via field-emission dielectric barrier discharge, Plasma Sources Sci. Technol. **27**, 085007 (2018).
[20] R. Fowler and L. Nordheim, Electron emission in intense electric fields, Proc. R. Soc. A **119**, 173 (1928).
[21] E. L. Murphy and R. H. Good, Thermionic emission, field emission, and the transition region, Phys. Rev. **102**, 1464 (1956).
[22] R. Kosloff, Quantum thermodynamics: A dynamical viewpoint, Entropy **15**, 2100 (2013).
[23] R. Lambert and N. Makri, Memory propagator matrix for long-time dissipative charge transfer dynamics, Mol. Phys. **110**, 1967 (2012).
[24] L. Landau, To the theory of energy transmission in collisions, Phys. Z. Sov. **2**, 46 (1932).
[25] C. Zener, Non-adiabatic crossing of energy levels, Proc. R. Soc. London A **137**, 696 (1932).
[26] E. Stückelberg, Theory of inelastic collisions between atoms, using two simultaneous differential equations, Helv. Phys. Acta **5**, 369 (1932).
[27] R. Marcus, Chemical and electrochemical electron-transfer theory, Annu. Rev. Phys. Chem. **15**, 155 (1964).
[28] T. Brandes and T. Vorrath, Adiabatic transfer of electrons in coupled quantum dots, Phys. Rev. B **66**, 075341 (2002).
[29] F. Renzoni and T. Brandes, Charge transport through quantum dots via time-varying tunnel coupling, Phys. Rev. B **64**, 245301 (2001).
[30] J. R. Rubbmark, M. M. Kash, M. G. Littman, and D. Kleppner, Dynamical effects at avoided level crossings: A study of the landau-zener effect using rydberg atoms, Phys. Rev. A **23**, 3107 (1981).
[31] D. A. Harmin and P. N. Price, Incoherent time evolution on a grid of Landau-Zener anticrossings, Phys. Rev. A **49**, 1933 (1994).
[32] R. Wild, J. Benduhn, and L. Stollenwerk, Surface charge transport and decay in dielectric barrier discharges, J. Phys. D **47**, 435204 (2014).
[33] F. Massines, N. Gherardi, N. Naudé, and P. Ségur, Recent advances in the understanding of homogeneous dielectric barrier discharges, Eur. Phys. J. Appl. Phys. **47**, 22805 (2009).
[34] M. Li, C. Li, H. Zhan, J. Xu, and X. Wang, Effect of surface charge trapping on dielectric barrier discharge, Appl. Phys. Lett. **92**, 031503 (2008).
[35] Y. Akishev, G. Aponin, A. Balakirev, M. Grushin, V. Karalnik, A. Petryakov, and N. Trushkin, Memory and sustention of microdischarges in a steady-state DBD: Volume plasma or surface charge? Plasma Sources Sci. Technol. **20**, 024005 (2011).
[36] F. X. Bronold, H. Fehske, H. Kersten, and H. Deutsch, Surface States and the Charge of a Dust Particle in a Plasma, Phys. Rev. Lett. **101**, 175002 (2008).
[37] R. L. Heinisch, F. X. Bronold, and H. Fehske, Phonon-mediated sticking of electrons at dielectric surfaces, Phys. Rev. B **82**, 125408 (2010).
[38] R. L. Heinisch, F. X. Bronold, and H. Fehske, Electron surface layer at the interface of a plasma and a dielectric wall, Phys. Rev. B **85**, 075323 (2012).
[39] F. X. Bronold and H. Fehske, Absorption of an Electron by a Dielectric Wall, Phys. Rev. Lett. **115**, 225001 (2015).
[40] J. Soler, E. Artacho, J. Gale, A. García, J. Junquera, P. Ordejón, and D. Sánchez-Portal, The SIESTA method for *ab initio* order-N materials simulation, J. Phys.: Condens. Matter **14**, 2745 (2002).
[41] A. Garcıa, ATOM User Manual (https://departments.icmab.es/leem/siesta/tlv14/Manuals/atom.pdf, accessed Nov. 2018. Laboratory of Electronic Structure of Materials (LEEM), Materials Science Institute of Barcelona (ICMAB) (2008).
[42] D. M. Ceperley and B. J. Alder, Ground State of the Electron Gas by a Stochastic Method, Phys. Rev. Lett. **45**, 566 (1980).
[43] T. Frauenheim, G. Seifert, M. Elsterner, Z. Hajnal, G. Jungnickel, D. Porezag, S. Suhai, and R. Scholz, A self-consistent charge density-functional based tight-binding method for predictive materials simulations in physics, chemistry and biology, Phys. Status Solidi B **217**, 41 (2000).
[44] B. Aradi, B. Hourahine, and T. Frauenheim, DFTB+, a sparse matrix-based implementation of the DFTB method, J. Chem. Phys. A **111**, 5678 (2007), parameters found at www.dftb.org, accessed June 2016.
[45] J. Slater and G. Koster, Simplified LCAO method for the periodic potential problem, Phys. Rev. **94**, 1498 (1954).
[46] N. Delone and V. Krainov, ac stark shift of atomic energy levels, Phys. Usp. **42**, 669 (1999).
[47] H. Nakamura, *Nonadiabatic Transition: Concepts, Basic Theories and Applications* (World Scientific, Singapore, 2012).
[48] A. Dodin, S. Garmon, L. Simine, and D. Segal, Landau-zener transitions mediated by an environment: Population transfer and energy dissipation, J. Chem. Phys. **140**, 124709 (2014).
[49] J. Huneke, G. Platero, and S. Kohler, Steady-State Coherent Transfer by Adiabatic Passage, Phys. Rev. Lett. **110**, 036802 (2013).
[50] N. A. Sinitsyn, J. Lin, and V. Y. Chernyak, Constraints on scattering amplitudes in multistate Landau-Zener theory, Phys. Rev. A **95**, 012140 (2017).
[51] Y. Demkov and V. Ostrovsky, Crossing of two bands of potential curves, J. Phys. B **28**, 403 (1995).
[52] Q. Niu and M. G. Raizen, How Landau-Zener Tunneling Takes Time, Phys. Rev. Lett. **80**, 3491 (1998).
[53] Y. Demkov and V. Ostrovsky, The exact solution of the multistate Landau-Zener type model: The generalized bow-tie model, J. Phys. B **34**, 2419 (2001).
[54] N. V. Vitanov and B. M. Garraway, Landau-Zener model: Effects of finite coupling duration, Phys. Rev. A **53**, 4288 (1996).
[55] P. Ao and J. Rammer, Influence of Dissipation on the Landau-Zener Transition, Phys. Rev. Lett. **62**, 3004 (1989).
[56] D. Zueco, P. Hänggi, and S. Kohler, Landau-Zener tunneling in dissipative circuit QED, New J. Phys. **10**, 115012 (2008).
[57] J. Chelikowsky and M. Schlüter, Electron states in α-quartz: A self-consistent pseudopotential calculation, Phys. Rev. B **15**, 4020 (1977).
[58] Z. A. Weinberg, G. W. Rubloff, and E. Bassous, Transmission, photoconductivity, and the experimental band gap of thermally grown SiO_2 films, Phys. Rev. B **19**, 3107 (1979).
[59] E. Calabrese and W. B. Fowler, Electronic energy-band structure of α-quartz, Phys. Rev. B **18**, 2888 (1978).

[60] E. Wagenaars, R. Brandenburg, W. Brok, M. Bowden, and H. Wagner, Experimental and modeling investigations of a dielectric barrier discharge in low-pressure argon, J. Phys. D **39**, 700 (2006).

[61] R. Tschiersch, S. Nemschokmichal, M. Bogaczyk, and J. Meichsner, Surface charge measurements on different dielectrics in diffuse and filamentary barrier discharges, J. Phys. D **50**, 105207 (2017).

[62] M. Bogaczyk, R. Wild, L. Stollenwerk, and H. Wagner, Surface charge accumulation and discharge development in diffuse and filamentary barrier discharges operating in He, N_2 and mixtures, J. Phys. D **45**, 465202 (2012).

[63] C. Birdsall, Particle-in-cell charged-particle simulations, plus Monte Carlo collisions with neutral atoms, PIC-MCC, IEEE Trans. Plasma Sci. **19**, 65 (1991).